ACS APPLIED MATERIALS & INTERFACES

Research Article

Cite This: ACS Appl. Mater. Interfaces 2018, 10, 13218−13225

www.acsami.org

Local Conduction in $Mo_xW_{1-x}Se_2$: The Role of Stacking Faults, Defects, and Alloying

Pantelis Bampoulis,* Kai Sotthewes, Martin H. Siekman, and Harold J. W. Zandvliet

Physics of Interfaces and Nanomaterials, MESA+ Institute for Nanotechnology, University of Twente, P.O. Box 217, 7500AE Enschede, The Netherlands

Supporting Information

ABSTRACT: Here, we report on the surface conductivity of WSe_2 and $Mo_xW_{1-x}Se_2$ ($0 \leq x \leq 1$) crystals investigated with conductive atomic force microscopy. We found that stacking faults, defects, and chemical heterogeneities form distinct two-dimensional and one-dimensional conduction paths on the transition metal dichalcogenide surface. In the case of WSe_2, in addition to step edges, we find a significant amount of stacking faults (formed during the cleaving process) that strongly influence the surface conductivity. These regions are attributed to the alternation of the 2H and 3R polytypism. The stacking faults form regular 2D patterns by alternation of the underlying stacking order, with a periodicity that varies significantly between different regions and samples. In the case of $Mo_xW_{1-x}Se_2$, its conductivity has a localized nature, which depends on the underlying chemical composition and the Mo/W ratio. Segregation to W-rich and Mo-rich regions during the growth process leads to nonuniform conduction paths on the surface of the alloy. We found a gradual change of the conductivity moving from one region to the other, reminiscent of lateral band bending. Our results demonstrate the use of C-AFM as a nanoscopic tool to probe the electrical properties of largely inhomogeneous samples and show the complicated nature of the surface conductivity of TMDC alloys.

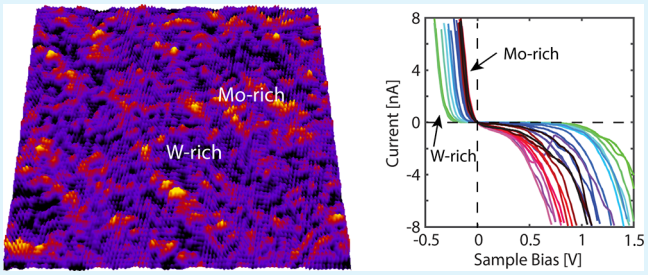

KEYWORDS: *$MoWSe_2$, transition metal dichalcogenide alloys, conductive AFM, heterojunctions, Schottky barrier, Fermi-level pinning, 2D semiconductor*

1. INTRODUCTION

Transition metal dichalcogenides (TMDC) have recently attracted a lot of attention because of their great promise in future nanoelectronics and their unique and tunable electronic structure.[1−4] TMDC materials consist of a transition metal layer, M, (e.g., Mo, W) sandwiched in between two covalently bonded chalcogen, X, layers (e.g., S, Se). These three atom-thick MX_2 layers are weakly bonded to each other via weak Van der Waals interactions. TMDC materials exhibit rich electronic properties that depend on the exact chemical composition, stacking order, and thickness of the material.[4−7] For example, bulk MoS_2 has an indirect band gap of about 1.3 eV, whereas monolayer MoS_2 has a direct band gap of 1.8−1.9 eV.[5,8,9] Similar behavior also occurs in other TMDCs such as WS_2 and WSe_2.[10−13] The tunability of their band gap along with their high quantum efficiency and optical adsorption has led to significant interest in optoelectronics.[9,14−17]

A promising way to tune the band gap and conduction band (CB)/valence band (VB) of TMDCs is by alloying.[11,18−22] Mixing Mo with W and S with Se is a delicate method to modulate the material's electronic structure.[22] The modulation strongly depends on the exact chemical composition and concentration of the constituent atoms.[18,22−24] For instance, single layers of $Mo_xW_{1-x}Se_2$ alloys have shown versatile physical properties, a tunable band gap, and CB/VB levels that depend on the exact ratio of Mo and W.[22,25] Although Mo and W have a similar electronic structure, there is a strong tendency during the growth process to phase-segregate into Mo-rich and W-rich regions,[13,20,25] leading to the formation of lateral heterojunctions. These regions often exhibit a one-dimensional (1D) character, forming striped patterns. The segregation was attributed to be a kinetically driven process, controlled by fluctuations occurring at the growth edge and the local availability of the chalcogen.[26]

In addition, TMDCs are often electronically inhomogeneous because of the presence of a high density of intrinsic defects and impurities.[27−31] For instance, substitution or removal of Mo or S atoms leads to defect sites with distinct electronic properties compared to pristine regions.[32] These sites alter the local electronic structure of MoS_2.[29] Apart from doping,[29] defects have also been shown to decrease locally the Schottky barrier height (SBH) with metal conducts, as a result of strong Fermi-level pinning,[33,34] and to lead to low-resistance conduction paths.[35] Furthermore, the contribution of edge states to the overall charge transport in TMDC films and crystals has not yet been fully understood. Edge states are

Received: January 26, 2018
Accepted: March 26, 2018
Published: March 26, 2018

DOI: 10.1021/acsami.8b01506
ACS Appl. Mater. Interfaces 2018, 10, 13218−13225

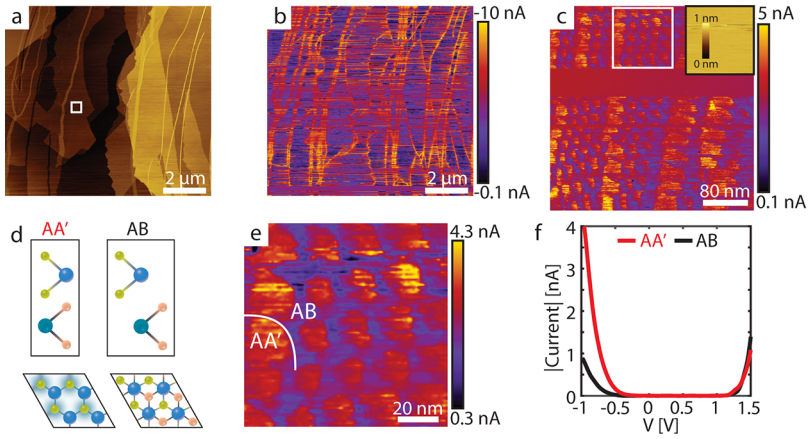

Figure 1. (a) Contact mode topography of the freshly cleaved WSe_2 surface. (b) Simultaneously recorded current image of the region in (a) SB is +0.5 V. (c) Small-scale C-AFM images recorded at the terrace marked with the white square in panel (a) with a SB of −0.9 V, showing a hexagonal lattice induced by stacking faults. The corresponding topography [inset of panel (c)] of the region shows no apparent height variations. (d) Side and top views of the ball and stick models of the AA′ and AB stacking orders. (e) Zoom-in image on the region marked with the white square at the stacking faults of panel (c), the AA′ and AB stacking orders are noted. (f) $I(V)$ characteristics of the AA′ and AB stacking orders.

induced by uncoordinated dangling bonds and the topology of the honeycomb lattice at the edges of the material and in the case of MoS_2 display a metallic character.[28,36−38]

The use of TMDCs and TMDC alloys in future (opto-)electronics will require the systematic understanding of their surface conductivity as well as charge transport with the metal contact. Variations in the stacking order and local composition could substantially influence this behavior. Therefore, understanding and controlling the electrical transport on van der Waals materials are crucial. So far, scanning tunneling microscopy (STM) is the main tool used for the characterization of the surface electronic structure of TMDCs.[29,39,40] In typical STM experiments, the measured signal is a combination of the surface's topography and density of states, and it is difficult to disentangle these two contributions. In contrast to STM, conductive atomic force microscopy (C-AFM) has the advantage that the measured conductivity is independent of the surface's topography. In addition, it can be used on surfaces with highly inhomogeneous conductivity.[41−43] However, C-AFM studies on TMDCs are scarce, and most of them are limited to spectroscopic investigations of the current−voltage ($I(V)$) characteristics of the tip sample[44−47] and lack the necessary spatial resolution. We have recently shown that C-AFM can be used to visualize defects on the MoS_2 surface with a diameter of a few nanometers.[33] In this study, the defects were only visible in the current image and were absent in the topographic images, suggesting that they are of electronic nature and induced by atom substitution/vacancy. In addition, we have shown that C-AFM is able to resolve nanoscopic charge puddles on graphene induced by intercalated ions.[48,49]

Despite the significant progress, the role of stacking faults, step edges, and alloying on the surface conductivity of TMDCs is largely unexplored. Here, we use C-AFM to characterize the conductivity of WSe_2 and $Mo_xW_{1-x}Se_2$ at the nanoscale. We find two-dimensional (2D) periodic patterns on the surface of WSe_2 reminiscent of stacking dislocations. Two characteristic domains are found that alternate with periodicity that varies across the sample. The two domains correspond to different stacking orders of the outermost WSe_2 layers. In addition, step edges exhibit higher currents than the rest of the surface. Finally, we demonstrate that C-AFM can provide images with atomic resolution, and we have explored the surface of different $Mo_xW_{1-x}Se_2$ alloys down to the atomic level. We observed segregation to Mo-rich and W-rich domains, which induces a strong anisotropy of the surface conductivity. We show that these two regions have distinct SBHs reflecting the different band structures of WSe_2 and $MoSe_2$.

2. RESULTS AND DISCUSSION

2.1. WSe_2: Step Edges and Stacking Faults. Figure 1a shows a freshly cleaved WSe_2 surface. For the sake of this study, we have intentionally chosen a part of the surface with several step edges (see Figure 1a). The simultaneously recorded C-AFM image (Figure 1b) reveals two distinct current levels for a sample bias of 0.5 V. It is evident that the WSe_2 step edges are significantly more conductive than the terraces. This observation is comparable with previous STM and density functional theory calculation studies, which show that MoS_2 step edges are metallic.[28,36−38] The most energetically favorable edges in MX_2 are the M-terminated zigzag (zz) edges and the X-terminated zz edges.[50] For instance, in MoS_2, Mo-zz and S-zz edges are commonly observed,[51] with Mo-zz edges being consistently sharper and straighter than S-zz edges.[52] Both Mo-zz and S-zz are metallic because of the presence of midgap states. Similar to MoS_2, we expect that this is most probably the cause of the higher conductivity observed in the current images reported here. The WSe_2 steps are unambiguously more conductive than the interior of the surface.

The noisy character of the large-scale C-AFM image does not allow us to investigate the conductivity of the terraces. To obtain detailed information regarding the surface conductivity, we zoom-in on a terrace of the region shown in Figure 1a. At this region (Figure 1c), a periodic pattern is visible in the C-AFM image. In contrast to C-AFM, the topographic image is rather flat, and it does not display any contrast at the corresponding location (see the inset of Figure 1c). Therefore, the contrast of the C-AFM cannot be attributed to missing WSe_2 layers or W/Se sublayers or any other structural features. It is known that synthetic WSe_2 (and other MX_2) displays two distinct polytypisms, the 2H phase (most common) and the 3R phase. The two phases differ from each other by sliding one of the two WSe_2 layers by one atomic unit. The stacking order and the alignment of both phases are shown in Figure 1d. The 2H phase is assigned as AA′ stacking and the 3R phase as AB

DOI: 10.1021/acsami.8b01506
ACS Appl. Mater. Interfaces 2018, 10, 13218−13225

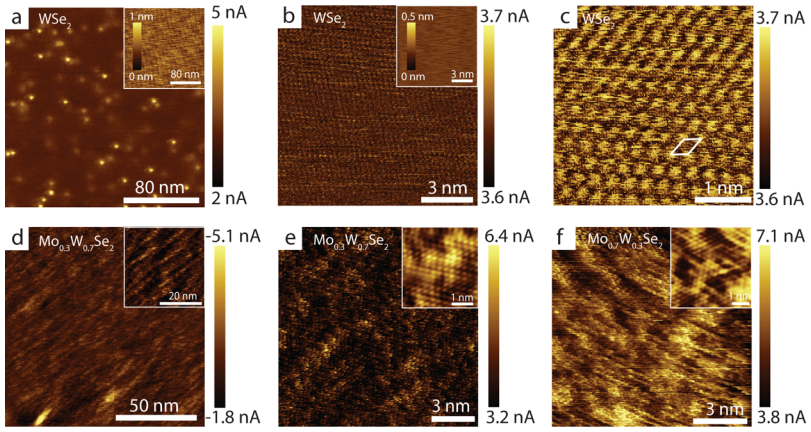

Figure 2. (a) C-AFM image of the WSe_2 surface with metal-like defects. Inset: the corresponding topography. (b) Small-scale C-AFM image of the WSe_2 surface. Inset: the corresponding topography. (c) Zoom-in image on (b) showing clear atomic periodicity in the C-AFM image. The periodicity amounts to 0.31 nm, in line with the lattice constant of WSe_2. The sample bias for (a–c) is −1 V. (d) Large-scale C-AFM image of the $Mo_{0.3}W_{0.7}Se_2$ surface; the current image is strongly heterogeneous. Inset: zoom-in image showing stripelike features. (e) Atomic-resolution C-AFM image of $Mo_{0.3}W_{0.7}Se_2$. Along with the current inhomogeneities, atomic periodicity is also visible. This is amplified in the zoom-in and low-pass filtered image shown in the inset. (f) Atomic-resolution C-AFM image of $Mo_{0.7}W_{0.3}Se_2$ showing both the atomic periodicity and the larger current variations. Inset: small-scale low-pass filtered image of the same region. The sample biases for (d–f) are 1.3 V, −0.9 V, and −1 V, respectively.

stacking.[53] Theoretical calculations revealed that the AA′ stacking order is by only 5 meV/unit more stable than the AB stacking order.[6] The small energy difference along with the weak Van der Waals bonds between adjacent layers should favor a network of stacking dislocations on the surface of WSe_2. This could in turn explain the above observations and the occurrence of the two distinct regions on the surface of WSe_2. Here, we exclude other types of stacking orders because they are energetically less stable.[6] The fact that we do not observe any height variations in the topographic images is in line with the theory that predicts the interlayer distance between the two configurations to be almost identical (0.650 nm for AA′ and 0.654 for AB).[6] Similar stacking dislocations have been previously reported on MoS_2 by transmission electron microscopy (TEM) imaging and on highly ordered pyrolytic graphite (HOPG) and multilayer graphene by the use of STM.[54−61]

The exact pattern of the alternating AA′ and AB regions depends on the preparation procedure and local strain variations.[58] To link the two regions to the right stacking order, we use the methodology described in ref 58. This approach uses the shape of the dislocations to extract the stacking order. The energy difference between the two regions results in a lateral pressure from the most favorable area to the least favorable area. This leads to the bending of the dislocation. Regions with a convex shape should correspond to the energetically favorable configuration. As can be seen from Figure 1e, the brighter regions have a convex shape, whereas the dimmer regions have a concave shape. Therefore, the brighter regions are linked to AA′ stacking and the dimmer to AB stacking.

Even though the observed stacking faults do not have any apparent influence on the topography of the WSe_2 surface, they strongly influence its conductivity. $I(V)$ measurements recorded on the two regions (Figure 1f) indeed reveal a distinct difference. The AA′ stacking exhibits larger currents for the forward bias [forward bias regime is defined when the sample (n-type semiconductor) is negatively biased] regime compared to the AB regions. However, this is in contrast to the band structure of the two phases, which is almost identical.[6] The identical band structure implies that $I(V)$ curves recorded on either of the two regions should be very similar. Considering that there are no differences in the band structure between the AA′ and AB stacking orders, the observed difference in the recorded $I(V)$ characteristics could be related to metal–semiconductor interface states formed inside the band gap,[62] which pin the Fermi level of the metal and influence the SBH of the junction.[33,34,63,64] These interface states might be located at different energy levels in the two phases and consequently pin the Fermi level at different energies, which would in turn result in different $I(V)$ characteristics. To properly understand this difference, a careful theoretical consideration is required, which is beyond the scope of this work.

2.2. $Mo_xW_{1-x}Se_2$: Alloying. In the following, we investigate the influence of alloying with Mo on the local conductivity of the TMDC surface. For this purpose, we have used $Mo_xW_{1-x}Se_2$ samples, where x = 0.7, 0.3, and 0. We will demonstrate that TMDC alloys host a tunable band gap and CB/VB levels, beneficial for many applications.[65] In these systems, both the Mo/W ratio and distribution are crucial and define the properties of the crystal.[22] It is therefore essential to understand their surface conductivity down to the nanometer scale. We will first start with the WSe_2 surface which is used as a reference sample. A current image recorded away from stacking faults and on the 2H WSe_2 has an almost homogeneous signal (Figure 2a). Circular features displaying higher currents are occasionally observed with a density that varies across the surface from 10^{10} to 10^{11} per cm^2. These features have been observed for several TMDCs in both C-AFM and STM images.[29,33,40,66] They have been interpreted as metal-like defects and are induced by atom substitution/vacancy on the outermost TMDC layers.[33] A zoom-in between these defects shows a smooth and flat surface in both the topography and the current image (see Figure 2b and its inset). In the current image, a periodic hexagonal pattern is also clearly visible (see Figure 2c). The pattern bears strong resemblance to atomic-resolution STM images of WSe_2, where a trigonal lattice is often observed and is attributed to the periodicity of the outermost Se layers.[67] Fast Fourier transformation of this image reveals a periodicity of about 0.31 nm, a value that matches well

DOI: 10.1021/acsami.8b01506
ACS Appl. Mater. Interfaces 2018, 10, 13218−13225

with the lattice periodicity of WSe_2 (see the Supporting Information). Simultaneously recorded lateral force microscopy (LFM) images show the same periodic pattern (see the Supporting Information). It is known that LFM can provide images with atomic periodicity because of stick and slip motion of the AFM tip with the atoms of the surface. Even though atomic resolution is readily obtained with STM, noncontact-AFM, and LFM, the resolution in C-AFM is normally in the nanometer range and atomic resolution has been reported only twice.[68,69] Similar periodic patterns have been obtained on HOPG;[68] however, because of the large tip radius, they were related to collective effects and not true atomic resolution. A recently submitted arXiv article[69] demonstrated that it is possible to obtain true atomic-resolution current images, when collective effects are avoided. Here, we have used a very sharp p-doped diamond tip with a radius of curvature less than 5 nm. A tip force in the order of 1−5 nN would lead to a contact area of about 0.4 nm^2. The small contact area suggests that the measured current passes through a subnanometer-sized region. On this basis, tip convolution should be limited and our images approach true atomic resolution. Nevertheless, the images clearly demonstrate that C-AFM can be used to resolve the conductivity of the surface down to the atomic level.

Having demonstrated that C-AFM can show local conductivity variations down to the atomic scale and that the 2H WSe_2 crystals have locally a rather homogeneous conductivity (apart from the presence of metal-like defects), we will now investigate the influence of different Mo concentrations on the electrical behavior of the surface. We have investigated two samples, a $Mo_{0.3}W_{0.7}Se_2$ and a $Mo_{0.7}W_{0.3}Se_2$ crystal. The obtained results for both systems are shown in Figure 2d−f. Similar to the results obtained on WSe_2, the topography and LFM images do not show any variations except the visible atomic periodicity (see the Supporting Information). However, the surface conductivity of the $MoWSe_2$ surface has a high degree of heterogeneity (see Figure 2d). The current images reveal not only an atomic modulation (see Figure 2e,f and their insets) but also distinct differences in the conduction of the material. For instance in Figure 2e, regions with significant higher currents are clearly visible. These regions increase in size and density for higher Mo concentrations ($x = 0.7$) (see Figure 2f). Because these regions are only visible in the alloy's surface and there is an increase of their areal density with increasing Mo concentration, it is suggested that they are induced by the presence of Mo in the crystal.

To understand the above observation, we have investigated with $I(V)$ spectroscopy the surface characteristics of the dim and bright regions, referred to as region (i) and region (ii), respectively (Figure 3a). As can be seen from the $I(V)$ characteristics of Figure 3b, there is a distinct difference in the conductivity of the two phases, with region (ii) being consistently more conductive than region (i).

The observed anisotropy on the C-AFM images and $I(V)$ characteristics of the $Mo_xW_{1-x}Se_2$ alloys points toward a phase segregation to Mo-rich and W-rich regions. Earlier TEM studies revealed that indeed TMDC alloys have the tendency to separate into Mo-rich and W-rich regions.[13,20,25] Interestingly, Azizi et al.[26] reported that phase segregation on TMDC alloys often leads to the formation of 1D chains (or stripes), and this observation was attributed to fluctuations occurring at the growth process. Similar patterns are also observed in our current images, as can be seen in the insets of Figure 2d,f. Here, we attribute the brighter regions [region (ii)] to Mo-rich

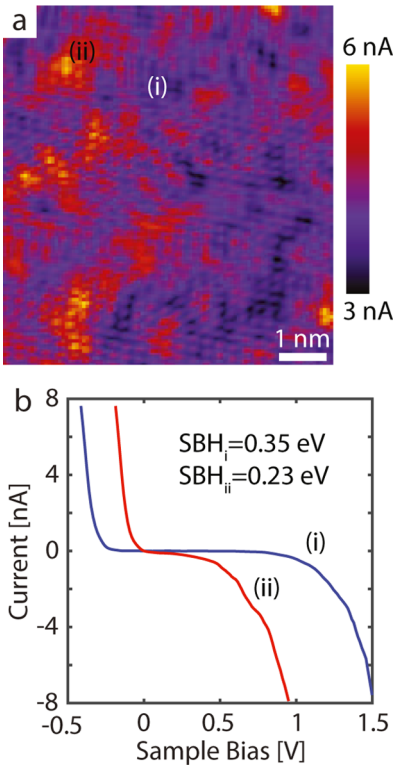

Figure 3. (a) C-AFM image of the $Mo_{0.3}W_{0.7}Se_2$ surface showing regions with different conductivities. (b) $I(V)$ characteristics recorded at region (i) and region (ii) of panel (a).

domains and the darker regions [region(i)] to W-rich domains. Indeed, the brighter regions not only scale with the Mo concentration but also provide higher currents. The phase segregation is a kinetically driven process, controlled by fluctuations occurring at the growth edge and the local availability of the chalcogen atoms.[26]

In principle, the contact between a metal and a semiconductor is either Ohmic or Schottky, depending on the difference between the metal work function and the semiconductor's work function. In the case of an n-type semiconductor, the contact is expected to be Ohmic when $\Phi_M < \Phi_S$ and Schottky when $\Phi_M > \Phi_S$, where Φ_M and Φ_S are the work functions of the metal and the semiconductor, respectively. In this case, $\Phi_M > \Phi_S$, and a Schottky contact is expected to occur between our highly doped diamond tips and the $Mo_xW_{1-x}Se_2$ samples, where a Schottky barrier is formed. Charge transport through a metal−semiconductor interface is typically described by thermionic emission, where the current I is given by

$$I = I_0\left[\exp\left(\frac{qV}{\eta k_B T}\right) - 1\right] \quad (1)$$

here, I_0 is the saturation current given by

$$I_0 = AA^*T^2 \exp\left(-\frac{q\phi_B}{k_B T}\right) \quad (2)$$

where A is the metal−semiconductor contact area, V is the applied bias voltage, T is the temperature (293 K), q is the electron charge, k_B is the Boltzmann constant, A^* is the Richardson constant ($A^* = 4\pi q m k_B^2/h^3$), and η is the ideality factor

DOI: 10.1021/acsami.8b01506
ACS Appl. Mater. Interfaces 2018, 10, 13218−13225

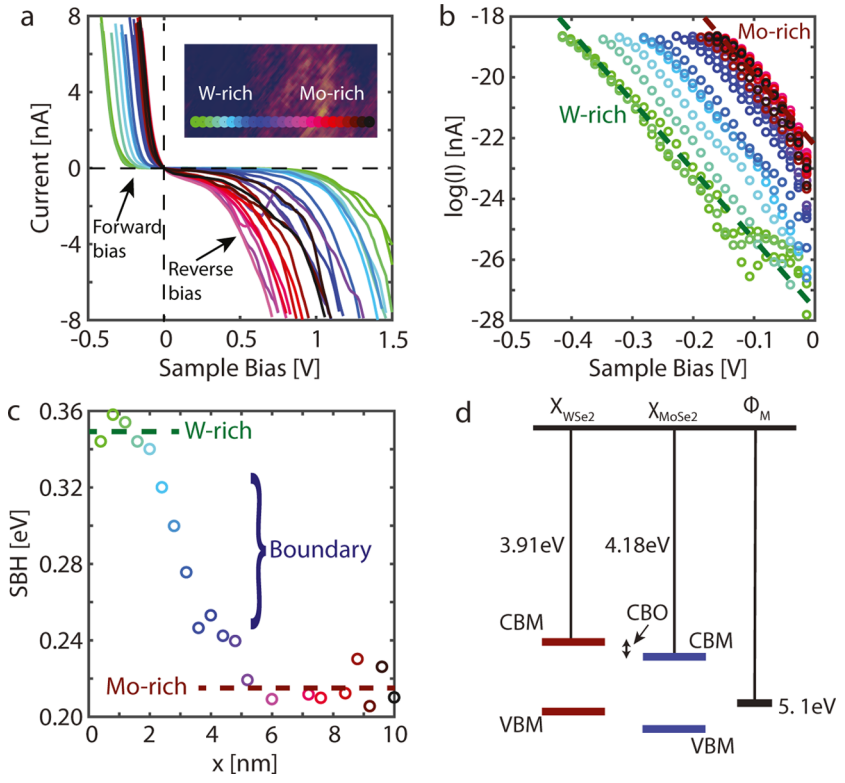

Figure 4. (a) $I(V)$ characteristics across a W-rich/Mo-rich boundary. The forward and reverse bias regimes are indicated in the panel. Inset: the W-rich and Mo-rich boundary; the rainbow line indicates the positions where the $I(V)$ characteristics were recorded. The color code corresponds to the exact $I(V)$ of panel (a). The log(I) vs V curves of panel (b) for the forward bias regime, showing the linear part where the fitting was done. (c) SBH as a function of the position, the color code corresponds to the exact $I(V)$ curves of panels (a,b). A clear transition is observed when moving from a W-rich region to a Mo-rich region. The transition is gradual and runs for about 3 nm. (d) CB minima and VB maxima of WSe_2 and $MoSe_2$ and the CBO.

$$\eta = \frac{q}{k_B T} \frac{dV}{d(\ln I)} \tag{3}$$

and the SBH (ϕ_B) is then given by

$$\phi_B = \frac{k_B T}{q} \ln\left(\frac{A^* A T^2}{I_0}\right) \tag{4}$$

The ideality factor is extracted from the slope of the linear part of the log(I)−V curve for the forward bias regime. The intercept of this fit gives the saturation current, which can be then used to extract the SBH according to eq 4. We find that the SBH is ∼0.35 eV for the W-rich regions and is ∼0.22 eV for the Mo-rich regions. The corresponding ideality factors are 1.6 and 1.4. The distinct difference in the SBH is in line with the different electron affinities of the $MoSe_2$ and WSe_2 semiconductors, where χ_{MoSe_2} (4.18 eV) > χ_{WSe_2} (3.91 eV)[3] (for the pure crystals). According to the Schottky−Mott rule and by direct comparison to the pure WSe_2 and $MoSe_2$ crystals, the Mo-rich regions should have a lower SBH than the W-rich regions and therefore be more conductive. This is indeed in line with our observations and supports our assignment of regions (i) and (ii) to W- and Mo-rich regions, respectively. However, the measured SBHs are far from the expected SBHs based on the Schottky−Mott rule. Similar observations have been reported before for MoS_2 and were attributed to Fermi-level pinning.[33,34]

Strikingly, the transition from one region to the other appears to be rather gradual. This is clearly shown in Figure 3a, where the centers of the Mo-rich domains are even more conductive. To explore this effect, we have recorded $I(V)$ characteristics (Figure 4a), along the line indicated in the inset which depicts the boundary between the Mo-rich and W-rich regions. Indeed, the $I(V)$ curves gradually change when moving from one region to the other. Figure 4b shows the logarithmic plots of the $I(V)$ curves for the forward bias regime. The extracted SBHs from the forward bias regime are shown in Figure 4c. The transition to the smaller SBH (Mo-rich) happens gradually and on the length scale of about 3−4 nm. This gradual transition is reminiscent of band bending across the phase boundary. The Mo-rich and W-rich regions are expected to approach the electronic band diagram of the $MoSe_2$ and WSe_2 crystals. The CB minimum and energy band gap of $MoSe_2$ and WSe_2, respectively, are shown in the schematic of Figure 4d. On the basis of this diagram, we expect to have locally a type-II staggered gap heterojunction when moving from a Mo-rich region to a W-rich region and band bending should occur at the interface of the two regions.[25] Assuming that the Fermi level pins at the same energy level across the boundary, the CB offset (CBO) can be estimated from the SBH difference between the two regions. We find a CBO of 0.13 eV. Here, we have neglected tip convolution because the transition takes place in a range much larger than the contact radius of the tip (∼0.4 nm).

Therefore, we have managed not only to visualize the atomic mixing in $Mo_xW_{1-x}Se_2$ alloys but also to quantify the influence of this mixing in their surface conductivity. We have shown that the metal−semiconductor SBH varies across the surface. This

DOI: 10.1021/acsami.8b01506
ACS Appl. Mater. Interfaces 2018, 10, 13218−13225

variation strongly depends on the underlying composition of the alloy and reflects the different CB levels of Mo-rich and W-rich regions. W-rich regions have a larger SBH because of a higher CB level than Mo-rich regions. The higher CB level is in line with W which is heavier than Mo. The tunability of the surface conductivity of $Mo_xW_{1-x}Se_2$ alloys could provide new opportunities for electronic and optoelectronic applications.

3. CONCLUSIONS

To conclude, we have investigated the local surface conductivity of $Mo_xW_{1-x}Se_2$ alloys using C-AFM. When x = 0, the surface conductivity of WSe_2 is influenced by step edges and stacking faults, formed by the cleaving process. The step edges form 1D metallic paths, whereas alternation of the AA′ and AB stacking orders forms 2D patterns with distinct electrical properties. We found that the AA′ stacking order is more conductive than the less favorable AB stacking order. In addition, when $0 < x < 1$, we observe a strong tendency for phase segregation to Mo-rich and W-rich regions, with the Mo-rich regions being more conductive, owing to the larger electron affinity. We have measured a transition of the tip/surface SBH from 0.35 eV at the W-rich regions to 0.22 eV at the Mo-rich regions. The transition is gradual and spans a scale of about 3−4 nm, reminiscent of band bending. The extracted CBO is 0.13 eV. Our findings show that the surface conductivity of $Mo_xW_{1-x}Se_2$ crystals is rather complicated and dominated by morphological features of the outermost layers. In addition, we demonstrate that C-AFM is a very powerful tool to visualize and investigate conduction down to the atomic scale and of highly inhomogeneous samples.

4. METHODS

Here, we have used synthetic $Mo_xW_{1-x}Se_2$ samples obtained from HQ graphene (Groningen, The Netherlands), where x was 0, 0.3 and 0.7. The TMDC samples were mechanically cleaved and thereafter inserted into the environmental chamber of the AFM, where they were continuously purged with N_2 gas, such that water contamination is avoided.[70] AFM imaging was done in contact mode with Agilent 5100 (Agilent) and Keysight 9500 (Keysight) AFM using conductive AFM probes (highly boron-doped diamond tips (AD-E-0.5-SS, Adama Innovations Ltd., resistivity: 0.003−0.005 Ω cm) with a nominal spring constant of 0.5 N/m and a resonance frequency of 30 kHz). LFM images were obtained simultaneously with topographic images by measuring the lateral torsion of the cantilever. For current imaging, the tip was grounded and a bias voltage was applied at the TMDC sample.

■ ASSOCIATED CONTENT

Supporting Information

The Supporting Information is available free of charge on the ACS Publications website at DOI: 10.1021/acsami.8b01506.

Experimental configuration, X-ray photoelectron spectroscopy spectrum, 2H and 3R phases, and atomic periodicity (PDF)

■ AUTHOR INFORMATION

Corresponding Author

*E-mail: p.bampoulis@utwente.nl.

ORCID

Pantelis Bampoulis: 0000-0002-2347-5223

Kai Sotthewes: 0000-0003-2073-6958

Funding

P.B. and H.J.W.Z. thank the Stichting voor Fundamenteel Onderzoek der Materie (FOM, FV157 14TWDO07) for financial support.

Notes

The authors declare no competing financial interest.

■ REFERENCES

(1) Wang, Q. H.; Kalantar-Zadeh, K.; Kis, A.; Coleman, J. N.; Strano, M. S. Electronics and Optoelectronics of Two-Dimensional Transition Metal Dichalcogenides. *Nat. Nanotechnol.* **2012**, *7*, 699−712.

(2) Xu, M.; Liang, T.; Shi, M.; Chen, H. Graphene-Like Two-Dimensional Materials. *Chem. Rev.* **2013**, *113*, 3766−3798.

(3) Rasmussen, F. A.; Thygesen, K. S. Computational 2D Materials Database: Electronic Structure of Transition-Metal Dichalcogenides and Oxides. *J. Phys. Chem. C* **2015**, *119*, 13169−13183.

(4) Duan, X.; Wang, C.; Pan, A.; Yu, R.; Duan, X. Two-Dimensional Transition Metal Dichalcogenides as Atomically Thin Semiconductors: Opportunities and Challenges. *Chem. Soc. Rev.* **2015**, *44*, 8859−8876.

(5) Mak, K. F.; Lee, C.; Hone, J.; Shan, J.; Heinz, T. F. Atomically Thin MoS_2: A New Direct-Gap Semiconductor. *Phys. Rev. Lett.* **2010**, *105*, 136805.

(6) He, J.; Hummer, K.; Franchini, C. Stacking Effects on the Electronic and Optical Properties of Bilayer Transition Metal Dichalcogenides MoS_2, $MoSe_2$, WS_2, and WSe_2. *Phys. Rev. B: Condens. Matter Mater. Phys.* **2014**, *89*, 075409.

(7) Wang, H.; Yuan, H.; Hong, S. S.; Li, Y.; Cui, Y. Physical and Chemical Tuning of Two-Dimensional Transition Metal Dichalcogenides. *Chem. Soc. Rev.* **2015**, *44*, 2664−2680.

(8) Splendiani, A.; Sun, L.; Zhang, Y.; Li, T.; Kim, J.; Chim, C.-Y.; Galli, G.; Wang, F. Emerging Photoluminescence in Monolayer MoS_2. *Nano Lett.* **2010**, *10*, 1271−1275.

(9) Radisavljevic, B.; Radenovic, A.; Brivio, J.; Giacometti, V.; Kis, A. Single-Layer MoS_2 Transistors. *Nat. Nanotechnol.* **2011**, *6*, 147−150.

(10) Huang, Y.; Sutter, E.; Sadowski, J. T.; Cotlet, M.; Monti, O. L. A.; Racke, D. A.; Neupane, M. R.; Wickramaratne, D.; Lake, R. K.; Parkinson, B. A.; Sutter, P. Tin Disulfide—An Emerging Layered Metal Dichalcogenide Semiconductor: Materials Properties and Device Characteristics. *ACS Nano* **2014**, *8*, 10743−10755.

(11) Kobayashi, Y.; Mori, S.; Maniwa, Y.; Miyata, Y. Bandgap-Tunable Lateral and Vertical Heterostructures Based on Monolayer $Mo_{1-x}W_xS_2$ Alloys. *Nano Res.* **2015**, *8*, 3261−3271.

(12) Zheng, S.; Sun, L.; Yin, T.; Dubrovkin, A. M.; Liu, F.; Liu, Z.; Shen, Z. X.; Fan, H. J. Monolayers of $W_xMo_{1-x}S_2$ Alloy Heterostructure with in-Plane Composition Variations. *Appl. Phys. Lett.* **2015**, *106*, 063113.

(13) Susarla, S.; Kochat, V.; Kutana, A.; Hachtel, J. A.; Idrobo, J. C.; Vajtai, R.; Yakobson, B. I.; Tiwary, C. S.; Ajayan, P. M. Phase Segregation Behavior of Two-Dimensional Transition Metal Dichalcogenide Binary Alloys Induced by Dissimilar Substitution. *Chem. Mater.* **2017**, *29*, 7431−7439.

(14) Yin, Z.; Li, H.; Li, H.; Jiang, L.; Shi, Y.; Sun, Y.; Lu, G.; Zhang, Q.; Chen, X.; Zhang, H. Single-Layer MoS_2 Phototransistors. *ACS Nano* **2011**, *6*, 74−80.

(15) Radisavljevic, B.; Whitwick, M. B.; Kis, A. Integrated Circuits and Logic Operations Based on Single-Layer MoS_2. *ACS Nano* **2011**, *5*, 9934−9938.

(16) Wang, H.; Yu, L.; Lee, Y.-H.; Shi, Y.; Hsu, A.; Chin, M. L.; Li, L.-J.; Dubey, M.; Kong, J.; Palacios, T. Integrated Circuits Based on Bilayer MoS_2 Transistors. *Nano Lett.* **2012**, *12*, 4674−4680.

(17) Lopez-Sanchez, O.; Lembke, D.; Kayci, M.; Radenovic, A.; Kis, A. Ultrasensitive Photodetectors Based on Monolayer MoS_2. *Nat. Nanotechnol.* **2013**, *8*, 497−501.

(18) Xi, J.; Zhao, T.; Wang, D.; Shuai, Z. Tunable Electronic Properties of Two-Dimensional Transition Metal Dichalcogenide Alloys: a First-Principles Prediction. *J. Phys. Chem. Lett.* **2013**, *5*, 285−291.

DOI: 10.1021/acsami.8b01506
ACS Appl. Mater. Interfaces 2018, 10, 13218−13225

(19) Chen, Y.; Xi, J.; Dumcenco, D. O.; Liu, Z.; Suenaga, K.; Wang, D.; Shuai, Z.; Huang, Y.-S.; Xie, L. Tunable Band Gap Photoluminescence from Atomically Thin Transition-Metal Dichalcogenide Alloys. *ACS Nano* **2013**, *7*, 4610−4616.
(20) Huang, C.; Wu, S.; Sanchez, A. M.; Peters, J. J. P.; Beanland, R.; Ross, J. S.; Rivera, P.; Yao, W.; Cobden, D. H.; Xu, X. Lateral Heterojunctions within Monolayer $MoSe_2$−WSe_2 Semiconductors. *Nat. Mater.* **2014**, *13*, 1096−1101.
(21) Zhang, M.; Wu, J.; Zhu, Y.; Dumcenco, D. O.; Hong, J.; Mao, N.; Deng, S.; Chen, Y.; Yang, Y.; Jin, C.; Chaki, S. H.; Huang, Y.-S.; Zhang, J.; Xie, L. Two-Dimensional Molybdenum Tungsten Diselenide Alloys: Photoluminescence, Raman Scattering, and Electrical Transport. *ACS Nano* **2014**, *8*, 7130−7137.
(22) Kutana, A.; Penev, E. S.; Yakobson, B. I. Engineering Electronic Properties of Layered Transition-Metal Dichalcogenide Compounds Through Alloying. *Nanoscale* **2014**, *6*, 5820−5825.
(23) Song, J.-G.; Ryu, G. H.; Lee, S. J.; Sim, S.; Lee, C. W.; Choi, T.; Jung, H.; Kim, Y.; Lee, Z.; Myoung, J.-M.; Dussarrat, C.; Lansalot-Matras, C.; Park, J.; Choi, H.; Kim, H. Controllable Synthesis of Molybdenum Tungsten Disulfide Alloy for Vertically Composition-Controlled Multilayer. *Nat. Commun.* **2015**, *6*, 7817.
(24) Feng, Q.; Zhu, Y.; Hong, J.; Zhang, M.; Duan, W.; Mao, N.; Wu, J.; Xu, H.; Dong, F.; Lin, F.; Jin, C.; Wang, C.; Zhang, J.; Xie, L. Growth of Large-Area 2D $MoS_{2(1-x)}Se_{2x}$ Semiconductor Alloys. *Adv. Mater.* **2014**, *26*, 2648−2653.
(25) Yoshida, S.; Kobayashi, Y.; Sakurada, R.; Mori, S.; Miyata, Y.; Mogi, H.; Koyama, T.; Takeuchi, O.; Shigekawa, H. Microscopic Basis for the Band Engineering of $Mo_{1-x}W_xS_2$-Based Heterojunction. *Sci. Rep.* **2015**, *5*, 14808.
(26) Azizi, A.; Wang, Y.; Lin, Z.; Wang, K.; Elias, A. L.; Terrones, M.; Crespi, V. H.; Alem, N. Spontaneous Formation of Atomically Thin Stripes in Transition Metal Dichalcogenide Monolayers. *Nano Lett.* **2016**, *16*, 6982−6987.
(27) Liu, D.; Guo, Y.; Fang, L.; Robertson, J. Sulfur Vacancies in Monolayer MoS_2 and its Electrical Contacts. *Appl. Phys. Lett.* **2013**, *103*, 183113.
(28) Zhou, W.; Zou, X.; Najmaei, S.; Liu, Z.; Shi, Y.; Kong, J.; Lou, J.; Ajayan, P. M.; Yakobson, B. I.; Idrobo, J.-C. Intrinsic Structural Defects in Monolayer Molybdenum Disulfide. *Nano Lett.* **2013**, *13*, 2615−2622.
(29) Addou, R.; Colombo, L.; Wallace, R. M. Surface Defects on Natural MoS_2. *ACS Appl. Mater. Interfaces* **2015**, *7*, 11921−11929.
(30) Addou, R.; McDonnell, S.; Barrera, D.; Guo, Z.; Azcatl, A.; Wang, J.; Zhu, H.; Hinkle, C. L.; Quevedo-Lopez, M.; Alshareef, H. N.; Colombo, L.; Hsu, J. W. P.; Wallace, R. M. Impurities and Electronic Property Variations of Natural MoS2 Crystal Surfaces. *ACS Nano* **2015**, *9*, 9124−9133.
(31) Addou, R.; Wallace, R. M. Surface Analysis of WSe_2 Crystals: Spatial and Electronic Variability. *ACS Appl. Mater. Interfaces* **2016**, *8*, 26400−26406.
(32) Hong, J.; Hu, Z.; Probert, M.; Li, K.; Lv, D.; Yang, X.; Gu, L.; Mao, N.; Feng, Q.; Xie, L.; Zhang, J.; Wu, D.; Zhang, Z.; Jin, C.; Ji, W.; Zhang, X.; Yuan, J.; Zhang, Z. Exploring Atomic Defects in Molybdenum Disulphide Monolayers. *Nat. Commun.* **2015**, *6*, 6293.
(33) Bampoulis, P.; van Bremen, R.; Yao, Q.; Poelsema, B.; Zandvliet, H. J. W.; Sotthewes, K. Defect Dominated Charge Transport and Fermi Level Pinning in MoS_2/Metal Contacts. *ACS Appl. Mater. Interfaces* **2017**, *9*, 19278−19286.
(34) Guo, Y.; Liu, D.; Robertson, J. Chalcogen Vacancies in Monolayer Transition Metal Dichalcogenides and Fermi Level Pinning at Contacts. *Appl. Phys. Lett.* **2015**, *106*, 173106.
(35) McDonnell, S.; Addou, R.; Buie, C.; Wallace, R. M.; Hinkle, C. L. Defect-Dominated Doping and Contact Resistance in MoS_2. *ACS Nano* **2014**, *8*, 2880−2888.
(36) Bollinger, M. V.; Lauritsen, J. V.; Jacobsen, K. W.; Nørskov, J. K.; Helveg, S.; Besenbacher, F. One-Dimensional Metallic Edge States in MoS_2. *Phys. Rev. Lett.* **2001**, *87*, 196803.
(37) Wu, D.; Li, X.; Luan, L.; Wu, X.; Li, W.; Yogeesh, M. N.; Ghosh, R.; Chu, Z.; Akinwande, D.; Niu, Q.; Lai, K. Uncovering Edge States and Electrical Inhomogeneity in MoS2 Field-Effect Transistors. *Proc. Natl. Acad. Sci. U.S.A.* **2016**, *113*, 8583.
(38) Farmanbar, M.; Amlaki, T.; Brocks, G. Green's Function Approach to Edge States in Transition Metal Dichalcogenides. *Phys. Rev. B* **2016**, *93*, 205444.
(39) Liu, X.; Balla, I.; Bergeron, H.; Hersam, M. C. Point Defects and Grain Boundaries in Rotationally Commensurate MoS2 on Epitaxial Graphene. *J. Phys. Chem. C* **2016**, *120*, 20798−20805.
(40) Park, J. H.; Sanne, A.; Guo, Y.; Amani, M.; Zhang, K.; Movva, H. C. P.; Robinson, J. A.; Javey, A.; Robertson, J.; Banerjee, S. K.; Kummel, A. C. Defect Passivation of Transition Metal Dichalcogenides via a Charge Transfer van der Waals Interface. *Sci. Adv.* **2017**, *3*, No. e1701661.
(41) Szot, K.; Speier, W.; Bihlmayer, G.; Waser, R. Switching the Electrical Resistance of Individual Dislocations in Single-Crystalline $SrTiO_3$. *Nat. Mater.* **2006**, *5*, 312−320.
(42) Basletic, M.; Maurice, J.-L.; Carrétéro, C.; Herranz, G.; Copie, O.; Bibes, M.; Jacquet, É.; Bouzehouane, K.; Fusil, S.; Barthélémy, A. Mapping the Spatial Distribution of Charge Carriers in $LaAlO_3$/$SrTiO_3$ Heterostructures. *Nat. Mater.* **2008**, *7*, 621−625.
(43) Rodenbücher, C.; Speier, W.; Bihlmayer, G.; Breuer, U.; Waser, R.; Szot, K. Cluster-like Resistive Switching of $SrTiO_3$: Nb Surface Layers. *New J. Phys.* **2013**, *15*, 103017.
(44) Giannazzo, F.; Fisichella, G.; Piazza, A.; Agnello, S.; Roccaforte, F. Nanoscale Inhomogeneity of the Schottky barrier and Resistivity in MoS_2 Multilayers. *Phys. Rev. B: Condens. Matter Mater. Phys.* **2015**, *92*, 081307.
(45) Giannazzo, F.; Fisichella, G.; Piazza, A.; Di Franco, S.; Oliveri, I. P.; Agnello, S.; Roccaforte, F. Current Injection from Metal to MoS_2 Probed at Nanoscale by Conductive Atomic Force Microscopy. *Mater. Sci. Semicond. Process.* **2016**, *42*, 174−178.
(46) Kaushik, V.; Varandani, D.; Das, P.; Mehta, B. R. On the Nature of AFM tip Metal-MoS_2 contact; Effect of Single Layer Character and Tip Force. *Appl. Phys. Lett.* **2017**, *111*, 141601.
(47) Song, S. H.; Joo, M.-K.; Neumann, M.; Kim, H.; Lee, Y. H. Probing Defect Dynamics in Monolayer MoS_2 via Noise Nanospectroscopy. *Nat. Commun.* **2017**, *8*, 2121.
(48) Bampoulis, P.; Sotthewes, K.; Siekman, M. H.; Zandvliet, H. J. W.; Poelsema, B. Graphene Visualizes the Ion Distribution on Air-Cleaved Mica. *Sci. Rep.* **2017**, *7*, 43451.
(49) Sotthewes, K.; Bampoulis, P.; Zandvliet, H. J. W.; Lohse, D.; Poelsema, B. Pressure-Induced Melting of Confined Ice. *ACS Nano* **2017**, *11*, 12723−12731.
(50) Byskov, L. S.; Nørskov, J. K.; Clausen, B. S.; Topsøe, H. Edge termination of MoS_2 and CoMoS catalyst particles. *Catal. Lett.* **2000**, *64*, 95−99.
(51) Lauritsen, J. V.; Kibsgaard, J.; Helveg, S.; Topsøe, H.; Clausen, B. S.; Lægsgaard, E.; Besenbacher, F. Size-Dependent Structure of MoS_2 Nanocrystals. *Nat. Nanotechnol.* **2007**, *2*, 53−58.
(52) van der Zande, A. M.; Huang, P. Y.; Chenet, D. A.; Berkelbach, T. C.; You, Y.; Lee, G.-H.; Heinz, T. F.; Reichman, D. R.; Muller, D. A.; Hone, J. C. Grains and Grain Boundaries in Highly Crystalline Monolayer Molybdenum Disulphide. *Nat. Mater.* **2013**, *12*, 554−561.
(53) Constantinescu, G.; Kuc, A.; Heine, T. Stacking in Bulk and Bilayer Hexagonal Boron Nitride. *Phys. Rev. Lett.* **2013**, *111*, 036104.
(54) Snyder, S. R.; Gerberich, W. W.; White, H. S. Scanning-Tunneling-Microscopy Study of Tip-Induced Transitions of Dislocation-Network Structures on the Surface of Highly Oriented Pyrolytic Graphite. *Phys. Rev. B: Condens. Matter Mater. Phys.* **1993**, *47*, 10823.
(55) Takahashi, N.; Shiojiri, M. Stacking Faults in Hexagonal and Rhombohedral MoS_2 Crystals Produced by Mechanical Operation in Relation to Lubrication. *Wear* **1993**, *167*, 163−171.
(56) Kobayashi, Y.; Takai, K.; Fukui, K.-i.; Enoki, T.; Harigaya, K.; Kaburagi, Y.; Hishiyama, Y. STM Observation of Electronic Wave Interference Effect in Finite-Sized Graphite with Dislocation-Network Structures. *Phys. Rev. B: Condens. Matter Mater. Phys.* **2004**, *69*, 035418.

DOI: 10.1021/acsami.8b01506
ACS Appl. Mater. Interfaces 2018, 10, 13218−13225

(57) Brown, L.; Hovden, R.; Huang, P.; Wojcik, M.; Muller, D. A.; Park, J. Twinning and Twisting of Tri- and Bilayer Graphene. *Nano Lett.* **2012**, *12*, 1609−1615.
(58) Hattendorf, S.; Georgi, A.; Liebmann, M.; Morgenstern, M. Networks of ABA and ABC Stacked Graphene on Mica Observed by Scanning Tunneling Microscopy. *Surf. Sci.* **2013**, *610*, 53−58.
(59) Enyashin, A. N.; Bar-Sadan, M.; Houben, L.; Seifert, G. Line Defects in Molybdenum Disulfide Layers. *J. Phys. Chem. C* **2013**, *117*, 10842−10848.
(60) Butz, B.; Dolle, C.; Niekiel, F.; Weber, K.; Waldmann, D.; Weber, H. B.; Meyer, B.; Spiecker, E. Dislocations in Bilayer Graphene. *Nature* **2014**, *505*, 533−537.
(61) Kisslinger, F.; Ott, C.; Heide, C.; Kampert, E.; Butz, B.; Spiecker, E.; Shallcross, S.; Weber, H. B. Linear Magnetoresistance in Mosaic-Like Bilayer Graphene. *Nat. Phys.* **2015**, *11*, 650−653.
(62) Cowley, A. M.; Sze, S. M. Surface States and Barrier Height of Metal-Semiconductor Systems. *J. Appl. Phys.* **1965**, *36*, 3212−3220.
(63) Kim, C.; Moon, I.; Lee, D.; Choi, M. S.; Ahmed, F.; Nam, S.; Cho, Y.; Shin, H.-J.; Park, S.; Yoo, W. J. Fermi Level Pinning at Electrical Metal Contacts of Monolayer Molybdenum Dichalcogenides. *ACS Nano* **2017**, *11*, 1588−1596.
(64) Gong, C.; Colombo, L.; Wallace, R. M.; Cho, K. The unusual Mechanism of Partial Fermi Level Pinning at Metal−MoS_2 Interfaces. *Nano Lett.* **2014**, *14*, 1714−1720.
(65) Yi, S.-G.; Kim, S. H.; Park, S.; Oh, D.; Choi, H. Y.; Lee, N.; Choi, Y. J.; Yoo, K.-H. $Mo_{1-x}W_xSe_2$-Based Schottky Junction Photovoltaic Cells. *ACS Appl. Mater. Interfaces* **2016**, *8*, 33811−33820.
(66) Rosenberger, M. R.; Chuang, H.-J.; McCreary, K. M.; Li, C. H.; Jonker, B. T. Electrical Characterization of Discrete Defects and Impact of Defect Density on Photoluminescence in Monolayer WS_2. *ACS Nano* **2018**, *12*, 1793−1800.
(67) Yao, Q.; van Bremen, R.; Zandvliet, H. J. W. Growth of Silicon on Tungsten Diselenide. *Appl. Phys. Lett.* **2016**, *109*, 243105.
(68) Enachescu, M.; Schleef, D.; Ogletree, D. F.; Salmeron, M. Integration of Point-Contact Microscopy and Atomic-Force Microscopy: Application to Characterization of Graphite/Pt(111). *Phys. Rev. B: Condens. Matter Mater. Phys.* **1999**, *60*, 16913.
(69) Rodenbücher, C.; Bihlmayer, G.; Speier, W.; Kubacki, J.; Wojtyniak, M.; Rogala, M.; Wrana, D.; Krok, F.; Szot, K. Detection of Confined Current Paths on Oxide Surfaces by Local-Conductivity Atomic Force Microscopy with Atomic Resolution. **2016**, arXiv:1611.07773. arXiv preprint.
(70) Bampoulis, P.; Teernstra, V. J.; Lohse, D.; Zandvliet, H. J. W.; Poelsema, B. Hydrophobic Ice Confined Between Graphene and MoS_2. *J. Phys. Chem. C* **2016**, *120*, 27079−27084.

DOI: 10.1021/acsami.8b01506
ACS Appl. Mater. Interfaces 2018, 10, 13218−13225